Mechanics of Advanced Composite Structures

Journal homepage: https://macs.semnan.ac.ir/

Semnan University

ISSN: 2423-7043

Research Article

Nonlinear Behavior of Honeycomb Structure Under Large Deformations Using Absolute Nodal Coordinate Formulation and Periodic Homogenization

Hossein Ranjbarzadeh, Seyed Mohammad Reza Khalili, Seyed Hossein Sadati

Center of Research for Composite and Smart Materials and Structures, Faculty of Mechanical Engineering, K. N. Toosi University of Technology, Tehran, Iran

ARTICLE INFO

Article history:

Received: 2023-10-19
Revised: 2024-03-22
Accepted: 2024-05-12

Keywords:

Honeycomb structure;
Absolute nodal coordinate formulation;
Periodic boundary conditions;
large deformation;
Elastic constants.

ABSTRACT

This study determines the elastic constants and evaluates the in-plane mechanical behavior of hexagonal and re-entrant (auxetic) honeycomb structures under large deformations by utilizing the Absolute Nodal Coordinate Formulation (ANCF) for modeling elastic forces and applying periodic boundary conditions (PBCs) to precisely control deformations at the boundaries. A representative volume element (RVE) was selected, and static equations were derived by modeling cell walls as beam elements using the ANCF based on the finite element method (FEM) and the periodic boundary conditions were subsequently implemented. After solving the static equations, analytical validation was performed for small deformations. The results demonstrate that honeycomb structures exhibit nonlinear behavior under large deformations, which is crucial to determine for dynamic applications. In addition, the proposed model provides an effective technique for determining elastic constants and evaluating the mechanical behavior of honeycomb structures under large deformations, with applicability to various cellular geometries and piezoelectric cell structures.

1. Introduction

Cellular solids play critical roles across diverse engineering applications. Advances in engineering design have enabled the development of multifunctional materials with capabilities exceeding those of conventional materials, particularly cellular architectures exhibiting superior properties including low density, enhanced energy absorption, tunable static moduli, efficient heat transfer, and unique acoustic behavior [1].

Among these, honeycomb structures—especially auxetic variants with negative Poisson's ratios—demonstrate exceptional characteristics through controlled structural deformations, enabling applications in impact absorption, thermal management, vibration damping, and military industries. While cellular materials are intrinsically anisotropic, their honeycomb configurations induce orthotropic behavior, which allows for precise control of mechanical properties (elastic modulus, shear

* **Corresponding author.**
E-mail address: *smrkhalili2022@gmail.com*

Cite this article as:
Ranjbarzadeh, H. Khalili, S.M.R. and Sadati, H., 2025. Nonlinear Behavior of Honeycomb Structure Under Large Deformations Using Absolute Nodal Coordinate Formulation and Periodic Homogenization. *Mechanics of Advanced Composite Structures*, 12(1), pp. xx-xx
https://doi.org/10.22075/MACS.2024.39315.2050

modulus, Poisson's ratio) through geometric parameterization.

Many studies in the literature have employed various methods to estimate elastic constants, including energy methods, stiffness matrix approaches, and conventional mechanical behavior analyses [2]. Gibson and Ashby [3] utilized classical theory and considered flexural deformation modes for cell walls under external loading. Their model has been widely referenced in subsequent studies investigating the dynamic and vibrational behavior of sandwich panels with honeycomb cores [4, 5]. Masters and Evans [6] developed a more comprehensive analytical model to predict elastic constants of honeycomb structures by incorporating flexural, stretching, and hinging deformation modes. Hedayati et al. [7] proposed a quarter-cell model and adopted a stiffness matrix methodology within both Euler-Bernoulli and Timoshenko theoretical frameworks to determine in-plane elastic constants of thick honeycomb structures. Chen and Ozaki [8] investigated the effect of core height on the in-plane elastic modulus of a hexagonal honeycomb core using the FE Method and proposed an analytical relation that directly calculates the elastic modulus (E_{22}) under the plane strain condition. It was shown that the elastic modulus of honeycomb structures is independent of height under the plane strain condition. Subsequently, Chen et al. [9] proposed theoretical formulas for calculating Young's modulus (E_{11}) and shear modulus (G_{12}). Sorohan et al. [10] studied a commercial hexagonal honeycomb structure with double vertical walls, accounting for sloped wall curvature, layer thickness, and adhesive fillet effects. They developed a new analytical method to model these structures. Furthermore, numerical simulations were performed both to validate the hypotheses underlying the analytical relationships and to identify limitations of the analytical model.

Significant advances in understanding auxetic mechanisms over recent decades have driven rapid diversification in engineered structures exhibiting negative Poisson's ratios. This expansion exploits multiple deformation principles to tailor material properties for application-specific requirements [11]. Prominent examples include double-arrowhead, STAR-n, trichiral, tetrachiral, hexachiral, anti-trichiral, and anti-tetrachiral configurations. For comprehensive theoretical frameworks, Reference [12] reviews methods for determining effective stress-strain behavior in 2D cellular materials with large-scale cells, establishing explicit relationships for linear elastic properties of fundamental geometries and introducing analytical methods for generalized cases. Reference [11] reports critical findings on the elastic properties of 2D auxetic honeycombs.

Recent studies demonstrate significant untapped potential for research and development in honeycomb structures. Illustrating this potential, Wang et al. [13] designed a hybrid hierarchical square honeycomb by first replacing each cell wall of a regular square honeycomb with smaller squares forming an edge-based hierarchical structure (EHSH) and then substituting every EHSH vertex with diamond substructures. This approach introduced tunable elastic moduli enabled by synergistic edge and vertex-level hierarchies. Critically, these results confirm that hybridizing and refining structural design features significantly enhances honeycomb mechanical performance. Extending this principle, Deng et al. [14] proved that combining hierarchical and gradient strategies in honeycomb-like structures markedly improves crashworthiness. Their work underscores the necessity of concurrently leveraging structural hierarchy and geometric gradients for lightweight, impact-resistant designs. Parallel innovations address fundamental property trade-offs: Wang et al. [15] recently developed interpenetrating phase composites using an aperiodic monotile truss lattice—inspired by Einstein's space-filling geometry, infiltrated with a polymer matrix. This design overcame the strength-toughness mutual exclusivity typical of lattice metamaterials, demonstrating the broader applicability of topological hybridization in architected materials.

Honeycomb structures exhibit nonlinear behavior when subjected to large deformations, such as in energy-absorbing or vibration-attenuation applications. Linear elasticity-based methods are insufficient for predicting the mechanical behavior of such structures, making it essential to characterize their nonlinear response [2]. Despite their importance, large deformations of honeycomb structures—particularly auxetic honeycombs—have received limited attention in the literature. Len et al. [16, 17] developed an analytical model to determine the in-plane mechanical properties of thin-walled honeycomb structures under both elastic and plastic deformation. Their results indicated that the structural response depends on equivalent stress, elastic modulus, and Poisson's ratio. Zhang et al. [18] investigated the nonlinear mechanical behavior of tetrahedral honeycomb structures and derived nonlinear correlations among normal stress, shear stress, Poisson's ratio, and strain under large deformations. Their findings revealed that Poisson's ratio behaves differently under large deformations compared to small strains. Additionally, axial loading was shown to

induce shear deformations in honeycomb structures. Fu et al. [19] introduced an analytical model to determine the in-plane shear modulus of hexagonal auxetic honeycombs under large deformations. They examined the effects of strain and cell geometry on the shear modulus and found that it increases with shear stress. Reducing the wall thickness led to a decrease in the shear modulus, while varying the cell wall inclination initially reduced the shear modulus, beyond which further reduction in inclination increased it again. Wang et al. [20] proposed a theoretical method to predict the negative Poisson's ratio of auxetic honeycombs under large deformations and studied the influence of geometric parameters. Their results demonstrated that Poisson's ratio does not remain constant and exhibits nonlinear behavior. Ma and Zhang [2] derived precise analytical equations for large deformations of auxetic honeycombs, including expressions for in-plane stress and strain, elastic modulus, and negative Poisson's ratio. A comparison with earlier studies on elastic constants showed that both approaches yielded nearly identical mechanical properties at strains below 0.02, with some reports offering even greater accuracy.

Literature review indicates that analytical models for nonlinear mechanical response remain predominantly confined to conventional hexagonal honeycomb and auxetic structures. Meanwhile, novel honeycomb designs continue to emerge to enhance mechanical performance. Consequently, analyzing the nonlinear behavior of these advanced configurations constitutes an active research frontier with persistent knowledge gaps. Given the increasing industrial adoption of highly-tunable architectures, developing precise methodologies to determine the nonlinear elastic-plastic characteristics of honeycomb cores has become critically imperative.

The FE method combined with periodic boundary conditions (PBCs) constitutes an effective approach for evaluating the mechanical behavior of honeycomb structures. PBCs provide more accurate estimates of effective moduli compared to uniform displacement and/or uniform traction boundary conditions [21]. In the analysis of structures comprising heterogeneous materials, homogenization techniques prove highly valuable for characterizing equivalent structural behavior under both small and large deformations. Within the multi-scale modeling framework, the representative volume element (RVE) has emerged as a widely adopted numerical strategy for homogenizing highly heterogeneous materials. This approach involves analyzing heterogeneous structures at the micro-scale to determine the overall behavior of the RVE, subsequently employing the obtained parameters in macro-models to predict the response of macroscopic structures under specified loading conditions [22]. The RVE typically represents a unit cell or a symmetric portion thereof, often subjected to prescribed displacements along its boundaries.

PBCs are implemented in RVEs by enforcing kinematic constraints on corresponding nodes, resulting in a periodically constrained displacement field. The RVE size must be sufficiently large to capture representative stress-strain responses, while the selection of appropriate boundary conditions plays a crucial role in determining homogeneous properties through finite element analysis (FEA) [23, 24]. Furthermore, displacement fields must be carefully selected for each load case based on actual deformation patterns. This approach requires periodic meshing such that each node on one RVE boundary possesses a corresponding counterpart on the opposite (periodic) boundary.

The demonstrated reliability of PBCs in RVE boundaries analysis for obtaining homogeneous properties has led to their extensive application in computational homogenization methods [23]. Sorohan et al. [25] developed both two-dimensional (2D) and three-dimensional (3D) FE models to investigate the equivalent orthotropic mechanical properties of honeycomb structures. These models were implemented using an RVE approach with efficiently applied PBCs for six distinct load cases in 3D simulations, enabling the determination of both in-plane and out-of-plane elastic properties of hexagonal honeycombs. The researchers employed various element types, including beam, 3D solid, and shell elements, in their modeling approach, with validation conducted through comparison with established analytical models from existing literature. The results demonstrated that such modeling frameworks can be effectively extended to various periodic cellular structures beyond honeycombs. Additionally, the methodology offers particular advantages for parametric studies due to its dependence on a limited number of geometric parameters. Cheng et al. [26] employed a computational homogenization technique based on the FE method to predict the effective elastic properties of honeycomb structures. FE results demonstrate consistent volume-average stress and boundary stress across diverse cell geometries and configurations. However, the strain energy method yields significantly different values for non-diagonal terms in the stiffness matrix compared to the volume-average method. Iyer et al. [27] and Khan et al. [28] employed the RVE method with efficient PBCs to determine the

electromechanical properties of auxetic piezoelectric cells.

Determining the mechanical behavior of cellular structures is critically important due to their extensive utilization as core elements in sandwich structures, where their properties are pivotal to the overall structural performance. Sandwich structures, comprised of two face sheets bonded to a lightweight cellular core, achieve remarkable structural efficiency by synergistically combining the bending resistance of the facings with the shear strength of the core. This design yields superior specific strength and stiffness. Recent studies have further confirmed that tailoring the cellular morphology allows for precise control over the mechanical response, including energy absorption and damage tolerance. Honeycomb structures, particularly auxetic honeycombs, are highly recommended as core materials due to their ability to leverage tunable porous architectures for exceptional energy absorption and impact resistance, often maintaining nearly constant stress levels under large compressive deformations across various loading directions [29]. Furthermore, employing honeycomb structures with optimized cellular parameters significantly enhances a range of mechanical properties, including impact resistance [29], dynamic response [30], nonlinear vibration characteristics [31], and vibration control performance [32].

In the present work, effective and efficient analytical models based on precise bending curvature relations are employed to estimate the mechanical behavior of both conventional and auxetic honeycomb structures under small and large deformations. The efficacy of these models stems from their ability to determine strain energy through the FE method coupled with PBCs, providing an accurate approach for obtaining the effective moduli of periodic structures. Accordingly, a unit cell was selected as the RVE of the honeycomb structure, and static equilibrium equations were extracted using the Absolute Nodal Coordinate Formulation (ANCF) within the FE framework. Subsequently, periodic homogenization was implemented under PBCs to determine effective moduli, Poisson's ratios, and nonlinear behavior of the honeycomb cell. The proposed framework is specifically designed to: (1) generalize predictions across diverse geometric configurations, including piezoelectric honeycombs; (2) capture finite-strain nonlinearity; and (3) maintain universal applicability to all auxetic architectures.

2. Derivation of the Static Governing Equations

2.1. Beam Model Description

The Euler-Bernoulli beam model applies to thin, slender beams where both rotational inertia and shear deformations are neglected. Accordingly, the cross-section of the undeformed beam is assumed to remain planar and normal to the neutral axis during deformation. This theory expresses the strain energy as:

$$U = \frac{1}{2}\int_V \sigma_x\, \varepsilon_x \mathrm{dV} \tag{1}$$

Strain energy variation is obtained as:

$$\delta U = \int_V \delta\varepsilon_x \sigma_x dV = \int_V E\,\varepsilon_x \delta\varepsilon_x dV \tag{2}$$

where ε_x denotes the axial strain. For any point on the cross-section of an Euler–Bernoulli beam, the axial strain is expressed as:

$$\varepsilon_x = \varepsilon_{x0} - y\kappa \tag{3}$$

where ε_{x0} is the axial strain along the neutral axis, while κ represents the curvature. Substituting eq. 3 into eq. 2 yields the variation of strain energy for a beam with uniform cross-section:

$$\delta U = \int_0^L EA\delta\varepsilon_{x0}\varepsilon_{x0} dx + \int_0^L EI\,\delta\kappa\,\kappa dx \tag{4}$$

2.2. Kinematics Relations of Absolute Nodal Coordinate Formulation

The stiffness matrix plays a pivotal role in both static and dynamic analysis of structures undergoing large deformations. Furthermore, the choice of coordinate system and underlying assumptions significantly influence the final solution. For instance, in Euler-Bernoulli beam theory under large deformations, two distinct coordinate systems denoted as "U" and "W" are commonly employed in beam modeling. Accordingly, the strain at the neutral axis and the curvature is expressed as follows [33]:

$$\varepsilon_0 = u' + \frac{1}{2}(u'^2 + w'^2) \tag{5}$$

$$\kappa = \frac{(1+u')w'' - u''w'}{\sqrt{(1+u')^2 + w'^2}} \tag{6}$$

where the second derivatives of "u" and "w" with respect to *x* must exist for curvature calculation. To discretize the equations using the FE method, third-order shape functions for "u" and "w" are required, defined as follows [34]:

$$N_u = [1 - 3\xi^2 + 2\xi^3, \mathrm{L}(\xi - 2\xi^2 + \xi^3), 0, 0, 3\xi^2 - 2\xi^3, \mathrm{L}(\xi^3 - \xi^2), 0, 0]$$

$$N_w = [0,0,1 - 3\xi^2 + 2\xi^3, \mathrm{L}(\xi - 2\xi^2 + \xi^3), 0,0,3\xi^2 - 2\xi^3, \mathrm{L}(\xi^3 - \xi^2)]$$

where $\xi = x/L$. An optimal modeling approach enhances accuracy, reduces the number of elements required for solution convergence [35], and improves computational efficiency in solving dynamic equations at high frequencies [36]. By incorporating Von-Kármán-type geometric nonlinearity while retaining the linear expression for bending curvature, the strain-displacement relationships is expressed as follows [34]:

$$\varepsilon_0 = u' + \frac{1}{2}(u'^2 + w'^2) \quad (7)$$

$$\kappa = w'' \quad (8)$$

It can be observed that the first derivatives of "u" and the second derivatives of "w" appear in the governing equations. Consequently, first-order shape functions may be employed for u*u*, defined as follows [34]:

$$N_u = [1 - \xi, ,0,0,\xi, 0,0]$$

$$N_w = [0,1 - 3\xi^2 + 2\xi^3, \mathrm{L}(\xi - 2\xi^2 + \xi^3), 0,3\xi^2 - 2\xi^3, \mathrm{L}(\xi^3 - \xi^2)]$$

This order reduction of finite elements and their linearization in bending curvature lead to reduced accuracy and necessitate an increased number of elements to achieve solution convergence.

Previous studies have indicated that the "U" and "W" coordinate frames, which employ displacement fields defined at high frequencies, exhibit numerical instabilities under very large deformations [36]. In contrast, the ANCF provides enhanced flexibility in the dynamic modeling of multi-body systems while maintaining high accuracy. This approach addresses stability concerns through the careful definition of boundary conditions and efficient constraint formulations. The use of third-order shape functions in the FE model for curvature representation simplifies the governing equations and achieves significantly improved solution accuracy [37]. The principal coordinate axis at point P on the neutral axis is defined as follows (see Fig. 1):

$$r = \begin{bmatrix} r_1 \\ r_2 \end{bmatrix} = Sq_e \quad (9)$$

where q_e is the nodal value vector:

$$q_e = [e_1 \ e_2 \ e_3 \ e_4 \ e_5 \ e_6 \ e_7 \ e_8]^T \quad (10)$$

The parameter e_i is given by:

$e_1 = r_1|_{x=0}$, $e_2 = r_2|_{x=0}$,

$e_5 = r_1|_{x=L}$, $e_6 = r_2|_{x=L}$,

$e_3 = r_{1,x}|_{x=0}$, $e_4 = r_{2,x}|_{x=0}$,

$e_7 = r_{1,x}|_{x=L}$, $e_8 = r_{2,x}|_{x=L}$

where L denotes the original length of the beam element. The shape function S is expressed as follows:

$$S = [s_1 I \quad s_2 I \quad s_3 I \quad s_4 I] \quad (11)$$

where I is a 2 × 2 identity matrix and s_i is given by:

$$s_1 = 1 - 3\xi^2 + 2\xi^3$$

$$s_2 = \mathrm{L}(\xi - 2\xi^2 + \xi^3)$$

$$s_3 = 3\xi^2 - 2\xi^3$$

$$s_4 = \mathrm{L}(\xi^3 - \xi^2)$$

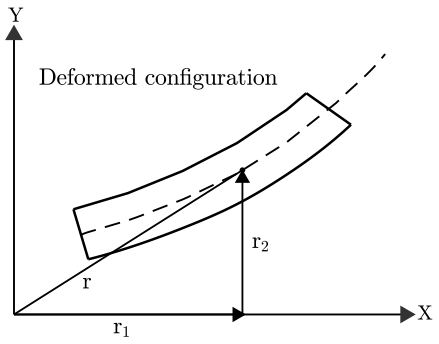

Fig. 1. Position vector of a given point on the neutral axis after deformation

The Green-Lagrange strain model for the neutral axis yields the following expression [38]:

$$\varepsilon_{x0} = \frac{1}{2}[r_{,x}{}^{\mathrm{T}} r_{,x} - 1] \quad (12)$$

Substituting eq. 9 into eq. 12, the axial strain and its variation for the e-th element are obtained as follows:

$$\varepsilon_{x0} = \frac{1}{2}(q_e^T S'^T S' q_e - 1) \quad (13)$$

$$\delta\varepsilon_{x0} = \delta q_e^T S'^T S' q_e \quad (14)$$

The curvature is written as [38]:

$$\kappa = \frac{r_{,x} \times r_{,xx}}{|r_{,x}|^3} \quad (15)$$

Substituting eq. 9 into eq. 15 yields:

$$\kappa = (S' q_e \times S'' q_e)/f^3 \quad (16)$$

where $f = \sqrt{q_e^T S'^T S' q_e}$. For a given neutral axis stretch with respect to the x-axis yields [38]:

$$\left|\frac{\partial s}{\partial x}\right| = \bar{f} = const, \tag{17}$$

$$f = \left|\frac{\partial r}{\partial x}\right| = \left|\frac{\partial r}{\partial s}\frac{\partial s}{\partial x}\right| = \bar{f}\left|\frac{\partial r}{\partial s}\right| \tag{18}$$

$$\left|\frac{\partial^2 r}{\partial s^2}\right| = \frac{1}{\bar{f}^2}\left|\frac{\partial^2 r}{\partial x^2}\right| \tag{19}$$

$$|\kappa|^2 = \frac{1}{\bar{f}^4}\left|r_{,xx}\right|^2 \tag{20}$$

$$\bar{f} = \sqrt{\int_0^L \delta q_e^T S'^T S' q_e dx} \tag{21}$$

Substituting eq. 9 into eq. 20, the curvature and its variation for the element is expressed as follows:

$$|\kappa|^2 = \frac{1}{\bar{f}^4}\delta q_e^T S''^T S'' q_e \tag{22}$$

$$\begin{aligned}\frac{1}{2}\delta(|\kappa|^2) = {} & \frac{1}{\bar{f}^4}\delta q_e^T S''^T S'' q_e \\ & - \frac{2}{\bar{f}^6}\delta q_e^T S''^T S'' q_e \\ & \cdot \int_0^L \delta q_e^T S'^T S' q_e dx\end{aligned} \tag{23}$$

2.3. Static Equations

The elastic force of element e can be obtained as [38]:

$$\begin{aligned}\delta Q_{fe} = {} & \frac{\delta U_e}{\delta q_e^T} \\ = {} & EA\int_0^L \varepsilon_{x0} S'^T S' dx\, q_e \\ & + EI\left[\frac{1}{\bar{f}^4}\int_0^L S''^T S'' dx\right. \\ & \left. - \frac{2}{\bar{f}^6}\int_0^L q_e^T S''^T S'' q_e\, dx \cdot \int_0^L S'^T S' dx\right] q_e\end{aligned} \tag{24}$$

The work of external forces (concentrated forces, distributed forces, and moments) can be defined as:

$$\delta W_e = \delta q_e^T Q_e \tag{25}$$

Using the variational form of D'Alembert-Lagrange's principle (i.e., the principle of virtual work), the governing equations for a flexible beam element can be derived as follows [39]:

$$\delta U_e + \delta W_e = 0 \tag{26}$$

Finally, the static equations of the beam element in the ANCF are rewritten as:

$$K(q_e)q_e = (K_r + K_t)q_e = Q_e \tag{27}$$

where K_r and K_t can be obtained from eq. 18 as follows [38]:

$$K = \frac{\partial Q_{fe}}{\partial q_e} \tag{28}$$

$$K_r = \int_0^L EA(S'^T S' q_e q_e^T S'^T S' - S'^T S')dx \tag{29}$$

$$\begin{aligned}K_t = {} & EI\left[\frac{1}{\bar{f}^4}\int_0^L S''^T S'' dx\right. \\ & \left. - \frac{2}{\bar{f}^6}\int_0^L q_e^T S''^T S'' q_e\, dx \cdot \int_0^L S'^T S' dx\right]\end{aligned} \tag{30}$$

After the assembling process for the flexible body, one gets the following expression:

$$K(a)a = Q_{ext} \tag{31}$$

where K is the global elastic stiffness matrix and Q_{ext} is the global vector of external forces. However, incorporating precise bending curvature relations results in a stiffness matrix that exhibits strong nonlinear dependence on nodal coordinates. Ultimately, the combination of higher-order elements and precise curvature computation enables high-fidelity numerical results.

The mechanical analysis of interconnected flexible bodies results in a system of constrained algebraic-differential equations. Consequently, the static equations are formulated using Lagrange multipliers as follows:

$$K(a)a + \lambda\Phi_{,a}^T(a) = Q_{ext} \tag{32}$$

$$\Phi(a) = 0 \tag{33}$$

where $\Phi_{,a}^T$ is the Jacobian matrix of constraints, while λ denotes the Lagrange coefficients.

It should be noted that, a limitation of this model is its assumption of linear elastic material behavior. While valid for the studied loading conditions, future work should incorporate nonlinear constitutive models (e.g., viscoelasticity [40]) to capture responses under extreme loading. The ANCF framework admits direct implementation of such advanced material formulations. Additionally, the influence of Poisson's ratio was not accounted for in the model.

2.4. Assembly of Stiffness Matrix and Force Vector

Figures 2(a) and 2(b) illustrate the auxetic honeycomb structures. The stiffness matrix K and force vector Q_{ext} for the auxetic honeycomb are defined by the following expressions:

$$K = \begin{bmatrix} K^{(1)} & 0 & \cdots & 0 \\ 0 & K^{(2)} & \cdots & 0 \\ \vdots & \vdots & \vdots & \vdots \\ 0 & 0 & \cdots & K^{(9)} \end{bmatrix},$$

$$a = \begin{bmatrix} q^{(1)} \\ q^{(2)} \\ \vdots \\ q^{(9)} \end{bmatrix}, Q_{ext} = \begin{bmatrix} Q^{(1)} \\ Q^{(2)} \\ \vdots \\ Q^{(9)} \end{bmatrix} \quad (34)$$

2.5. Constraints Definition in Body-Body Connection Zones

Slope discontinuities occur at the connections between adjacent bodies. Shabana and Mikkola [41] provided detailed constraint definitions for such configurations. Figure 2(c) depicts the connection between bodies 1 and 2, where ψ_1 and ψ_2 represent the initial angles of bodies 1 and 2 relative to the horizontal axis, respectively. This study employs the following constraint equations:

$$q_1^{(1)} = q_1^{(2)} \quad (35)$$

$$q_2^{(1)} = q_2^{(2)} \quad (36)$$

$$q_3^{(1)} - q_3^{(2)} = \cos(\psi_1) - \cos(\psi_2) \quad (37)$$

$$q_4^{(1)} - q_4^{(2)} = \sin(\psi_1) - \sin(\psi_2) \quad (38)$$

where the superscript denotes the body number, and the subscript indicates the nodal deformation. These constraint equations are applied to all body-body connection points within the honeycomb cellular structure.

2.6. PBCs

To implement PBCs for the RVE, a re-entrant honeycomb (auxetic) structure is adopted, as illustrated in Figure 2(d). Nodes N_1, N_2, N_3, and N_4 represent the corner and primary nodes, while nodes $Node_{YPos}$ and $Node_{YNeg}$ correspond to the upper and lower boundary nodes of the unit cell, respectively. The kinematic constraints between corresponding nodes is expressed as follows [21]:

$$Node_{YPos}^{(i)} - Node_{YNeg}^{(i)} + N_3 - N_1 = 0 \quad (39)$$

$$N_4 - N_3 - N_2 - N_1 = 0 \quad (40)$$

Based on Euler-Bernoulli beam theory and the nodal deformation vector (eq. 10), each node possesses four degrees of freedom (DOFs). Constraints eq. 39 and eq. 40 are applied to corresponding nodal pairs (e.g., q_1 and q_2 or q_5 and q_6). To eliminate rigid body motion, the displacement vector of node N_1 is constrained to zero. Dirichlet boundary conditions (Table 1) [21] are imposed to compute the effective elastic moduli and characterize the nonlinear behavior of the honeycomb structure under large deformations.

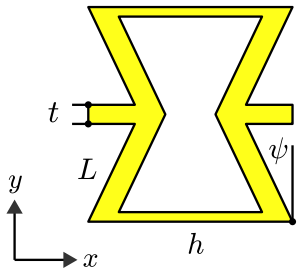

(a) Auxetic cell

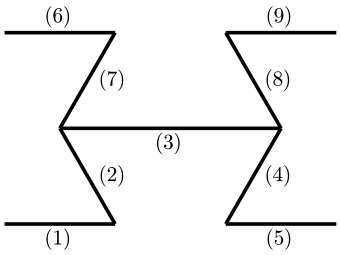

(b) Body numbering scheme

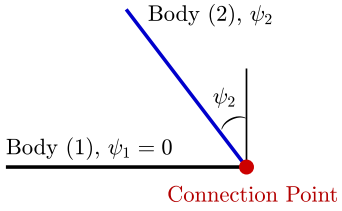

(c) Inter-body connectivity points

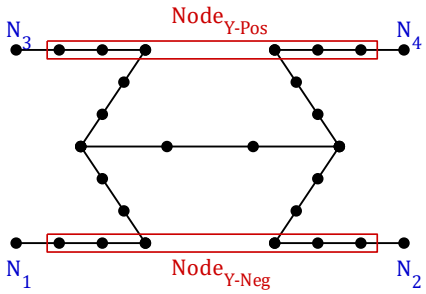

(d) Boundary and corner node designations

Fig. 2. Schematic of the auxetic honeycomb unit cell

The volume averaging technique is used to calculate the average stress and strain [21]:

$$\bar{\sigma}_{ij} = \frac{1}{V}\int_V \sigma_{ij}(x,y,z)dV \quad (41)$$

The average stress can be written as:

$$\bar{\sigma}_{ij} = \frac{F_{ij}}{A_j} \tag{42}$$

The average strain is given by:

$$\bar{\varepsilon} = \frac{\delta_i}{L_i} \tag{43}$$

3. Results and Discussion

The proposed model was validated against analytical models reported in the literature. The nonlinear behavior of both hexagonal and auxetic honeycomb structures was evaluated.

3.1. FE Model Validation

To ensure the simulation results are independent of mesh density, a mesh convergence analysis was conducted, as illustrated in Figures 3(a) and 3(b). The model parameters were set as follows: Young's modulus E = 70 GPa, unit cell dimensions L = h = 5 mm, thickness ratio t/L = 0.05, and re-entrant angle ψ = 30°. It can be observed that as the number of elements increases, the values of both E_{11} and E_{22} gradually decrease and converge at a mesh density of eight elements per body. Consequently, a mesh size of 0.625 mm (5 mm / 8 elements) was adopted for all subsequent analyses.

To evaluate the errors associated with classical analytical relations, the results obtained from the models of Gibson et al. [3], Masters and Evans [6], and Sorohan et al. [10] were compared with those from the present model under varying α_1 = t/L and α_2 = h/L ratios. The models by Sorohan et al. [10] and Masters and Evans [5], which incorporate flexural, stretching, and hinging deformation modes, show higher accuracy. To exclude the influence of Poisson's ratio, which cannot be accounted for in the current model, the value was set to ν = 0.

Table 2 presents the effective elastic properties of the auxetic honeycomb with parameters E = 70 GPa, α_2 = 1, α_1= 0.01, 0.05, 0.1, and ψ = 30° at 1% strain. Figure 4 illustrates the deformation mode of the auxetic unit cell under large deformations. Across all three models, the maximum errors occur for E_{11} and G_{12}. For α_1 = 0.01, these were overestimated by more than 6.2% and 18.79%, respectively. As the α_1 ratio increases to 0.05, the relative error decreases. The maximum underestimation observed in the model by Gibson et al. [3] was 4.54%. For α_1 = 0.1, the maximum overestimations for E_{11} and G_{12} were 7.52% and 15.82%, respectively. A similar trend is observed for the auxetic structure with parameters E = 70 GPa, α_2 = 1.5, α_1 = 0.05, and ψ = 30° at 1% strain (Table 2). The maximum error, an overestimate of 23.3%, was found in the model by Gibson et al. [3]. Furthermore, as the α_1 ratio increases, thereby enhancing the stiffness of the auxetic structure, the error in the shear modulus G_{12} also increases.

According to Tables 2 and 3, it can be concluded that the proposed model based on Euler-Bernoulli beam theory and employing the ANCF along with PBCs yields acceptable results for the elastic moduli E_{11}, E_{22}, and Poisson's ratios ν_{12}, ν_{21}. However, for the shear modulus G_{12}, considering the effect of cell parameters with various α_1 and α_2 ratios, a maximum error of 23.3% is observed. It should be noted that in the analytical models Masters and Evans [6], and Sorohan et al. [10], shear deformations are accounted in addition to bending and axial deformations, particularly in the model by Chen and Ozaki [8] and Chen et al. [9], the effect of cell height is considered, as a result leading to improved accuracy in estimating the shear modulus G_{12}. It may be suggested that extending the current model based on first-order or higher-order shear deformation theories, along with incorporating the effect of Poisson's ratio, would be necessary to draw more definitive conclusions in this regard.

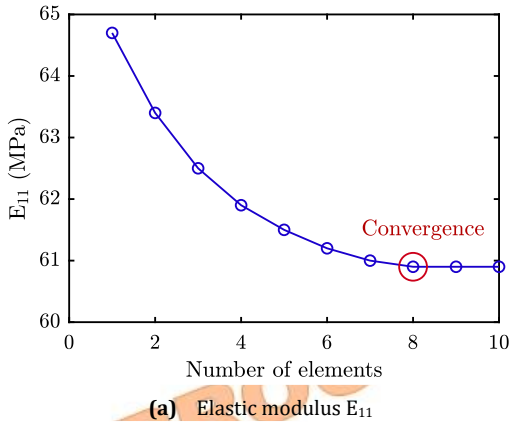

(a) Elastic modulus E_{11}

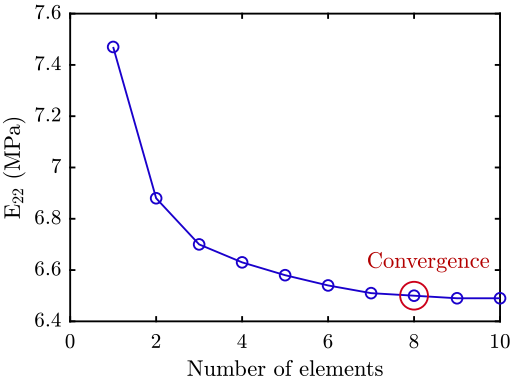

(b) Elastic modulus E_{22}

Fig. 3. Elastic modulus as a function of the element numbers

Table 1. Nodal constraints for PBCs [22]

Properties	Node N_2		Node N_3	
E_{11}, ν_{12}	$q^{(5)}_{(end-3)} = q^{(5)}_{(end-3)\_int} + \delta_x$,	$q^{(5)}_{(end-2)} = 0$	$q^{(6)}_1 = 0$	
E_{22}, ν_{21}	$q^{(5)}_{(end-2)} = 0$		$q^{(6)}_1 = 0$,	$q^{(6)}_2 = q^{(6)}_{(2)\_int} + \delta_y$
G_{12}	$q^{(5)}_{(end-3)} = q^{(5)}_{(end-3)\_int}$,	$q^{(5)}_{(end-2)} = \delta_y$	$q^{(6)}_1 = 0$,	$q^{(6)}_2 = 0$

Table 2. In-plane elastic properties for auxetic cell with E = 70 GPa, α_2 = 1 and b = 0.25L and ψ=30°

α_1	properties	Present	Gibson et al. [3]		Masters and Evans [6]		Sorohan et al. [10]	
			Value	Error (%)	Value	Error (%)	Value	Error (%)
0.01	E_{11}(MPa)	0.0539	0.0538	-0.19	0.0538	-0.19	0.0538	-0.19
	E_{22}(MPa)	0.516	0.484	-6.20	0.484	-6.20	0.485	-6.01
	G_{12}(MPa)	0.0165	0.0134	-18.79	0.0134	-18.79	0.0134	-18.79
	ν_{12}	-0.327	-0.333	1.83	-0.332	1.53	-0.333	1.83
	ν_{21}	-3.086	-3	-2.79	-2.988	-3.18	-2.998	-2.85
0.05	E_{11}(MPa)	6.54	6.73	2.91	6.64	1.53	6.64	1.53
	E_{22}(MPa)	60.9	60.62	-0.95	59.78	-2.32	59.81	-2.27
	G_{12}(MPa)	1.607	1.68	4.54	1.67	3.92	1.67	3.92
	ν_{12}	-0.3238	-0.33	1.91	-0.33	1.91	-0.33	1.91
	ν_{21}	-3.0716	-3	-2.33	-2.97	-3.31	-2.97	-3.31
0.1	E_{11}(MPa)	49.3	53.88	9.29	51.02	3.49	51.12	3.69
	E_{22}(MPa)	451	484.9	7.52	459.26	1.83	461.18	2.26
	G_{12}(MPa)	11.63	13.47	15.82	13.1	12.64	13.21	13.59
	ν_{12}	-0.3131	-0.3333	6.45	-0.3206	2.40	-0.3206	2.40
	ν_{21}	-3.031	-3	-1.02	-2.8835	-4.87	-2.8861	-4.78

Table 3. In-plane elastic properties for auxetic cell with E = 70 GPa, α_2 = 1.5 and b = 0.25L and ψ=30°

α_1	properties	Present	Gibson et al. [3]		Masters and Evans [6]		Sorohan et al. [10]	
			Value	Error (%)	Value	Error (%)	Value	Error (%)
0.01	E_{11}(MPa)	0.107	0.107	0.00	0.107	0.00	0.107	0.00
	E_{22}(MPa)	0.258	0.242	-6.20	0.242	-6.20	0.242	-6.20
	G_{12}(MPa)	0.0103	0.00898	-12.82	0.00898	-12.82	0.00897	-12.91
	ν_{12}	-0.6557	-0.666	1.57	-0.666	1.57	-0.666	1.57
	ν_{21}	-1.543	-1.5	-2.79	-1.499	-2.85	-1.499	-2.85
0.05	E_{11}(MPa)	13.07	13.47	3.06	13.47	3.06	13.23	1.22
	E_{22}(MPa)	30.75	30.3	-1.46	29.88	-2.83	29.87	-2.86
	G_{12}(MPa)	0.975	1.12	14.87	1.11	13.85	1.11	13.85
	ν_{12}	-0.6463	-0.666	3.05	-0.6579	1.79	-0.6579	1.79
	ν_{21}	-1.535	-1.5	-2.28	-1.4852	-3.24	-1.4552	-5.20
0.1	E_{11}(MPa)	97.42	107.77	10.62	100.7	3.37	100.5	3.16
	E_{22}(MPa)	226.37	242.4	7.08	229.63	1.44	229.09	1.20
	G_{12}(MPa)	7.28	8.98	23.35	8.88	21.98	8.85	21.57
	ν_{12}	-0.6211	-0.666	7.23	-0.6334	1.98	-0.6334	1.98
	ν_{21}	-1.5152	-1.5	-1.00	-1.4432	-4.75	-1.4433	-4.75

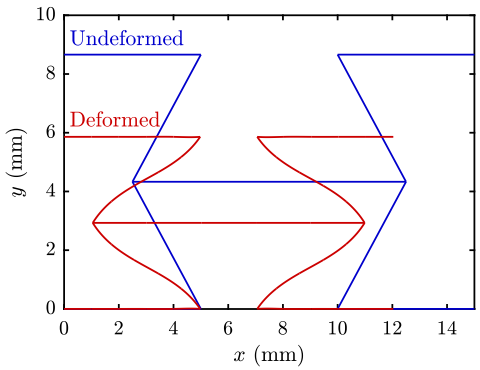

Fig. 4. Representative deformation behavior of the auxetic honeycomb structure under applied loading.

3.2. *Mechanical Response of the Honeycomb Under Deformation*

To evaluate the effect of deformations on the mechanical behavior of honeycomb structures, a hexagonal honeycomb cell with parameters α_1 = 0.1, α_2 = 1, b = 15 mm, and ψ = 30°, and an auxetic honeycomb with α_1 = 0.1, α_2 = 3, b = 15 mm, and ψ = 30° were analyzed at 10% strain. The elastic modulus E and Poisson's ratio ν were set to 1 GPa and 0.3, respectively.

Figures 5(a)–5(b) and 6(a)–6(b) present the stress-strain curves for the conventional and auxetic honeycomb cells, respectively. The initial slope of each curve represents the elastic modulus. The σ_{11}–ε_{11} curve exhibits slight nonlinearity for both honeycomb structures, which is attributed to the stiffness in this direction. The auxetic cell shows an ascending curve with a decreasing slope, while the conventional cell displays an ascending curve with an increasing slope. The σ_{22}–ε_{22} curve demonstrates an increasing trend with a positive slope for both honeycombs. The honeycombs exhibit moderate stiffness in this direction and more pronounced nonlinear behavior. A similar trend is observed for the shear modulus (Figs. 5(c) and 6(c)). Due to the system's stiffness in the x-direction, ν_{12} shows a linear correlation with stress (Figs. 5(d) and 6(d)). For the auxetic honeycomb, ν_{12} decreases as σ_{11} increases, whereas for the conventional honeycomb, ν_{12} increases with σ_{11}. Furthermore, an increase in τ_{12} results in a more significant change in ν_{21}.

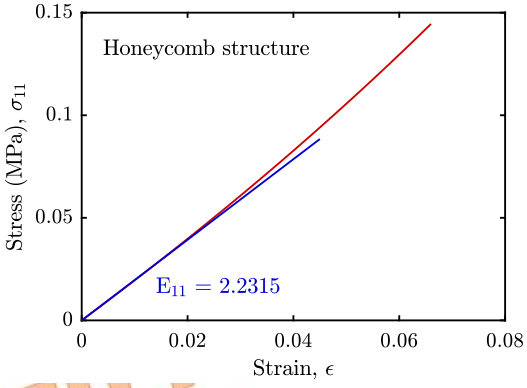

(a) Normal stress, σ_{11}

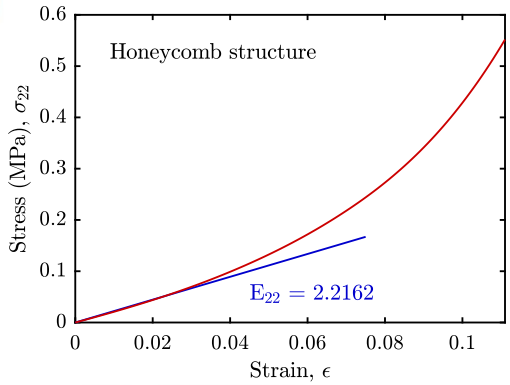

(b) Normal stress, σ_{22}

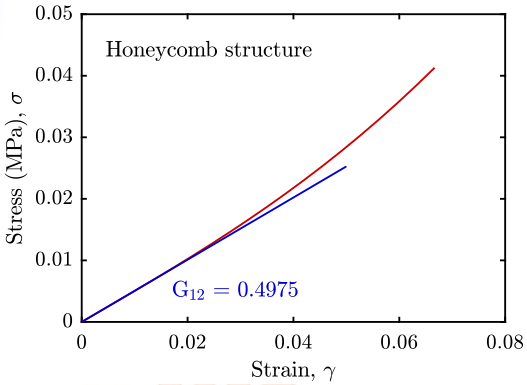

(c) Shear stress, τ_{12}

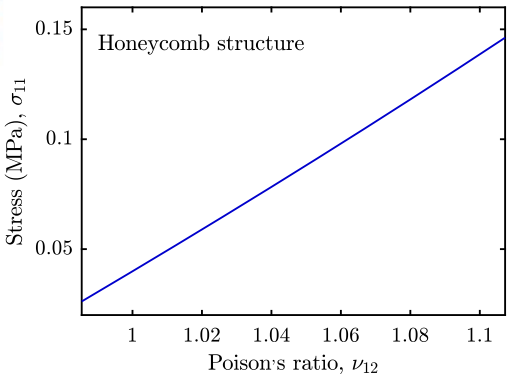

(d) Effective Poisson's ratio, ν_{12}

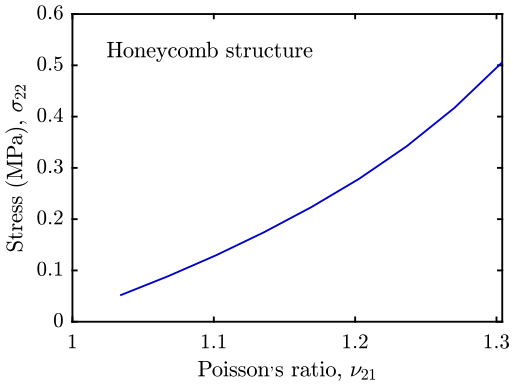

(e) Effective Poisson's ratio, $\boldsymbol{\nu_{21}}$

Fig. 5. Stress-strain curves for the hexagonal honeycomb structure

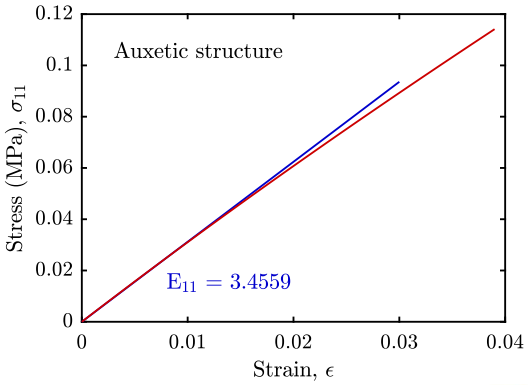

(a) Normal stress, σ_{11}

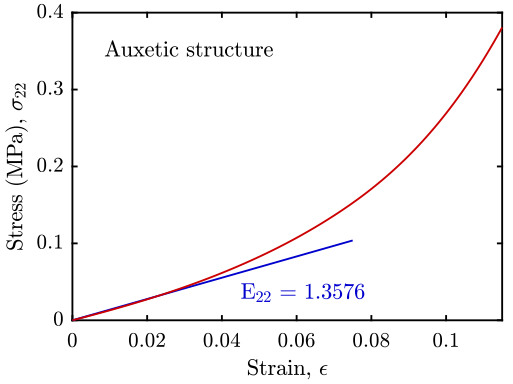

(b) Normal stress, σ_{22}

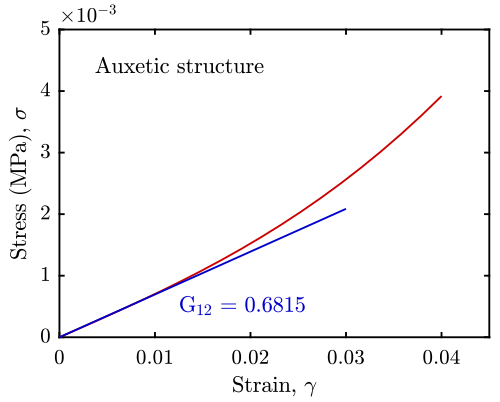

(c) Shear stress, τ_{12}

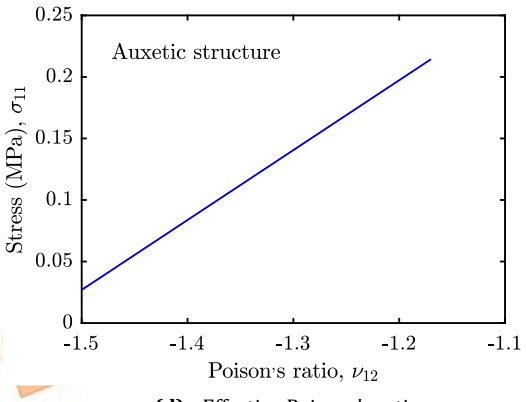

(d) Effective Poisson's ratio, ν_{12}

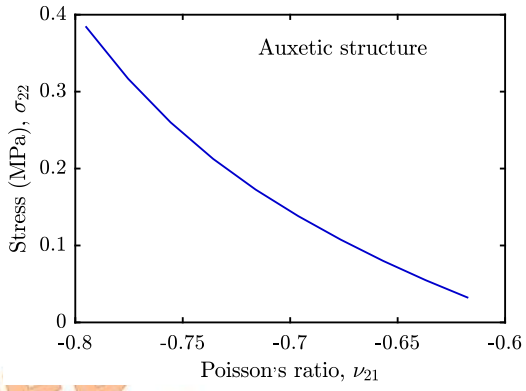

(e) Effective Poisson's ratio, ν_{21}

Fig. 6. Stress-strain curves for the re-entrant honeycomb structure

3.3. Effects of Auxetic Cell Geometric Parameters on the In-Plane Elastic Modulus

Due to their exceptional mechanical properties, auxetic honeycomb structures are vital for numerous applications. This study investigates the influence of two key geometric ratios on their elastic properties: the thickness-to-length ratio (α_1) and the cell length-to-lateral wall length ratio (α_2). The corresponding figures are plotted under the manufacturability constraint of 2h - 2L sin(ψ) ≥ 1.5 mm, which ensures the feasibility of fabricating the auxetic unit cell [42].

The results in Tables 2 and 3 show that increasing α_1 (0.01 to 0.1) substantially raises the elastic moduli, E_{11} (0.053 to 49.3 MPa), E_{22} (0.51 to 451 MPa), and G_{12} (0.0165 to 11.63 MPa). This trend is primarily attributed to the enhanced structural stiffness from thickness growth. In contrast, Poisson's ratios remain nearly constant, as the re-entrant angle was kept constant (ψ = 30°). A simultaneous increase in both α_1 (0.01 to 0.1) and α_2 (1 to 1.5) also elevates the elastic moduli, E_{11} (0.107 to 97.42 MPa), E_{22} (0.58 to 228.37 MPa), and G_{12} (0.0103 to 7.23 MPa). This

enhancing effect is more pronounced in structures with smaller cell lengths (h). A key observation is the significant sensitivity of E_{11} to α_2; the modulus increases from 49.3 to 97.42 MPa due to cell length enlargement. Here, the reduction of ε_{11} strain under constant stress yields a higher effective modulus. Under large deformations, the axial strains of members (1, 5, 6, and 9) dominate the behavior of E_{11}. In contrast, E_{22} decreases from 451 to 228.37 MPa along the y-direction. This reduction originates from the decrease in the stress-bearing area caused by the increase in cell length under a constant ε_{22} strain. At large deformations, the bending of members (1, 5, 6, and 9), in combination with the bending of the lateral walls, further contributes to the reduction of E_{22}.

The major advantage of the proposed model is its capability to precisely capture both axial and bending deformations. This makes the model a reliable tool for analyzing the large-deformation behavior of honeycomb structures.

Figure 7 presents the numerical simulation results characterizing the relationship between the normalized elastic modulus (E_{11}/E) and the re-entrant angle ψ across various α_1 and α_2 values. The data reveal a consistent monotonic enhancement of E_{11}/E with increasing ψ, a trend that becomes increasingly pronounced at higher angles, as indicated by the progressively steeper curves in both subfigures. This behavior demonstrates a substantial positive correlation between E_{11}/E and ψ under constant α_1 and α_2 conditions, consistent with established literature findings [43]. Additionally, comparative analysis of Figures 7(a) and 7(b) indicates that elevating either the aspect ratio α_1 or length ratio α_2, while maintaining a constant re-entrant angle ψ, increases the normalized elastic modulus E_{11}/E.

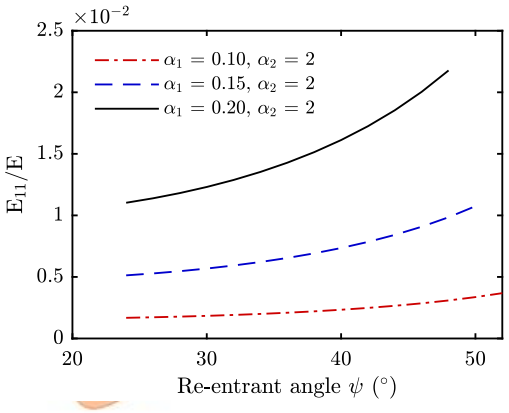

(a)

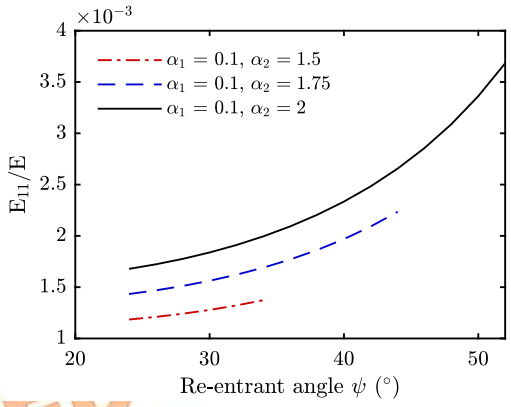

(b)

Fig. 7. The normalized elastic modulus E_{11}/E versus ψ

Figure 8 illustrates the numerical simulation results for the normalized elastic modulus (E_{22}/E). The results indicate that the normalized modulus E_{22}/E decreases with increasing re-entrant angle ψ. This decreasing trend is more pronounced at smaller re-entrant angles (ψ = 25°) compared to larger angles (ψ = 50°), where E_{22}/E exhibits minimal variation. This behavior is opposite to that observed for the modulus in the x-direction. As discernible from Figure 8(a), the normalized modulus E_{22}/E increases with α_1 when α_2 and the re-entrant angle ψ are held constant. This enhancement can be attributed to the improved resistance to bending deformation in the lateral walls resulting from increased thickness. Conversely, E_{22}/E exhibits an inverse relationship with α_2, indicating reduced structural stiffness with increasing length dimensions (Fig. 8(b)).

A comparison of the normalized moduli in the x- and y-directions reveals that E_{22} is generally larger than E_{11}, particularly at larger re-entrant angles. This indicates that the two-dimensional re-entrant auxetic structure can exhibit higher stiffness and resistance to loading along the y-direction. In general, the three independent geometric parameters ψ, α_1, and α_2 each exert a distinct influence on the elastic modulus of the auxetic structure.

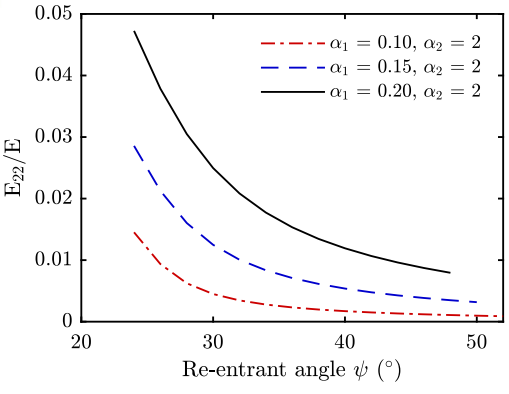

(a)

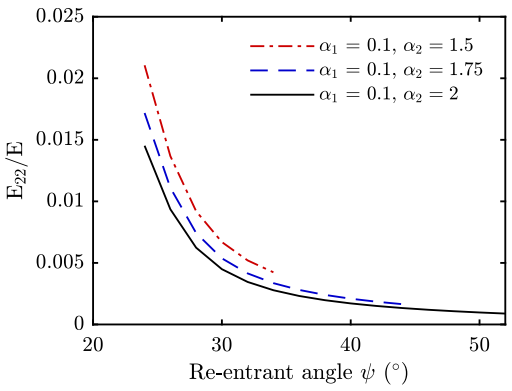

(b)

Fig. 8. The normalized elastic modulus E_{22}/E versus ψ

Figure 9 shows the variation of the effective Poisson's ratio ν_{12} with respect to the re-entrant angle ψ. As observed, ν_{12} remains negative and exhibits a nonlinear, monotonic increase as ψ increases. This increasing behavior becomes more pronounced at larger angles. For a constant angle ψ, an increase in α_1 leads to a further decrease in ν_{12} (Fig. 9(a)). In contrast, an increase in α_2 results in an increase in ν_{12}, although the overall increasing trend with ψ persists. Thus, a higher length ratio α_2 consistently increases the magnitude of the negative Poisson's ratio across all values of ψ.

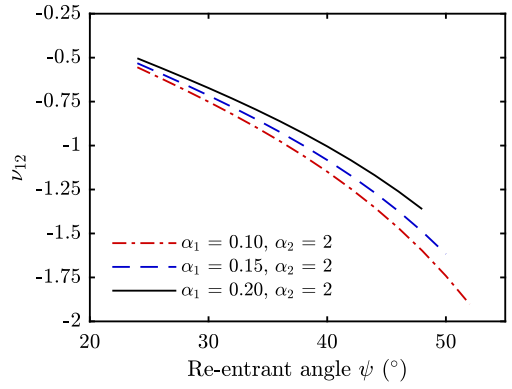

(a)

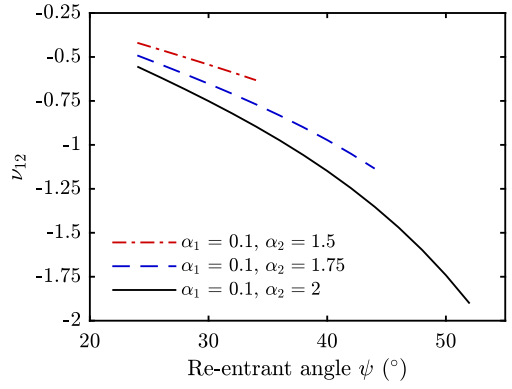

(b)

Fig. 9. The effective Poisson's ratios ν_{12} and ν_{21} versus ψ

Figure 10 presents the variation of the effective Poisson's ratio ν_{21} as a function of the re-entrant angle ψ. The results show an inverse correlation between ν_{21} and ψ, with Poisson's ratio decreasing as the re-entrant angle increases. As illustrated in Figure 10(a), ν_{21} exhibits a decreasing trend with increasing length ratio α_1 while maintaining constant α_2. Similarly, the aspect ratio α_2 demonstrates an inverse relationship with ν_{21}, where higher α_2 values correspond to reduced Poisson's ratio values. Comparative analysis reveals a directional dependence of Poisson's ratio behavior. For re-entrant angles below a specific threshold, ν_{21} consistently exceeds ν_{12} in magnitude. Furthermore, these two parameters indicate contrasting responses to variations in ψ, while ν_{12} decreases with reducing re-entrant angle, ν_{21} shows a corresponding increase.

The findings presented in this section align with the work of Wang et al. [43] and confirm that the proposed model is highly effective for capturing the nonlinear mechanical response of cellular structures.

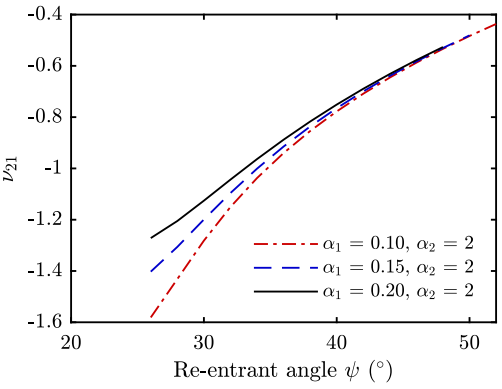

(a)

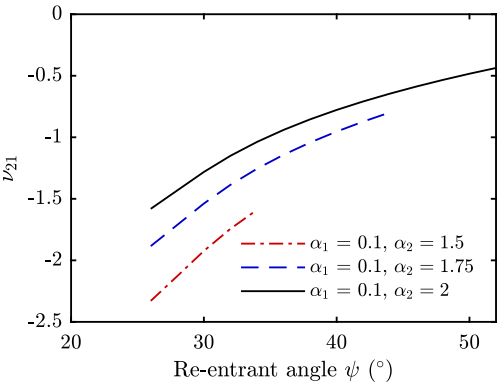

(b)

Fig. 10. The effective Poisson's ratio ν21 versus ψ

4. Conclusions

Honeycomb structures constitute a class of cellular materials whose mechanical properties can be strategically engineered through

meticulous design of their geometric parameters. The development of accurate computational models for predicting these properties is therefore essential. This study presents an advanced numerical framework that integrates the Absolute Nodal Coordinate Formulation (ANCF) with Periodic Boundary Conditions (PBC) to characterize in-plane elastic constants and capture nonlinear structural behavior under large deformations. The implementation of Euler-Bernoulli beam theory within the ANCF framework enables precise computation of elastic forces, while PBCs ensure physically realistic deformations at structural boundaries.

Comparative analyses with established analytical models demonstrate that the proposed approach provides superior accuracy in predicting elastic moduli (E_{11}, E_{22}) and Poisson's ratios (ν_{12}, ν_{21}), particularly for structures with varying thickness-to-length (t/L) and cell height-to-length (h/L) ratios. The maximum errors were obtained in predicting mechanical properties, about the elastic modulus E_{22} (6.2%) and the shear modulus G_{12} (21.79%). Given that more advanced analytical models (such as those by Masters and Evans [6] and Sorohan et al. [10]) simultaneously consider bending, tensile, and shear deformation modes for calculating the shear modulus, it can be concluded that drawing definitive conclusions regarding the accuracy of shear modulus predictions necessitates further development of the current model by incorporating shear deformation effects and Poisson's ratio. The parametric investigations reveal that mechanical properties exhibit significant nonlinear variations with changes in re-entrant angle (ψ) and dimensional ratios, emphasizing the necessity of precise modeling before practical application.

This model can be extended to cellular structures of different geometries as well as piezoelectric cell structures by incorporating voltage degrees of freedom. Future research will focus on enhancing the model's capability to accurately determine elastic constants and characterize nonlinear behavior under large deformations through the implementation of Timoshenko beam theory, which accounts for Poisson's ratio effects. Furthermore, extending the modeling framework to honeycomb structures with advanced material behaviors, such as shape-memory polymers and other nonlinear materials, represents a promising direction for future investigation.

Nomenclature

A	Beam cross-sectional area
E_{ij}	Elastic modulus
G_{ij}	Shear modulus
υ_{ij}	Poisson's ratio
x	Distance along the x-axis
ξ	Dimensionless length
u	Axial deflection of the beam
w	Lateral deflection of the beam
U	Strain energy
ε_{x0}	Axial along the neutral axis
κ	Bending curvature
e	Nodal value vector
S	Shape function
(')	Differentiation with respect to x
δ	Variational Derivative
Q_e	work of external forces
ψ_i	Cell wall angle
h	Length of the inclined rib
L	Length of the vertical cell rib
t	Thickness of the rib
λ	Lagrange multiplier
K_r	Axial stiffness matrix
K_t	Bending stiffness matrix

Acknowledgments

Special thanks to Prof. Seyed Mohammad Reza Khalili who is the head of the Mechanics Research Centre for Advanced and Intelligent Structures.

Funding Statement

This research did not receive any specific grant from funding agencies in the public, commercial, or not-for-profit sectors.

Conflicts of Interest

The author declares that there is no conflict of interest regarding the publication of this article.

References

[1] Ren, X., Das, R., Tran, P., Ngo, T.D., Xie, Y.M., 2018. Auxetic metamaterials and structures: A Review. *Smart Materials and Structures*, 2(7) 023001. doi: 10.1088/1361-665X/aaa61c.

[2] Ma, Q., Zhang, J., 2023. Nonlinear constitutive and mechanical properties of an auxetic honeycomb structure. *Mathematics*, 11(9), 2062. doi: 10.3390/math11092062.

[3] Gibson, L.J., Ashby, M.F., Schajer, G.S., Roberson, C.I., 1982. The mechanics of two-dimensional cellular materials. Proc. *R. Soc. Lond. A*. 382, pp. 25–42. doi: 10.1098/rspa.1982.0087.

[4] Nguyen, D.D., Pham, H.C., 2018. Nonlinear dynamic response and vibration of composite plates with negative Poisson's ratio in auxetic honeycombs. *Journal of Sandwich Structures and Materials*, 20(6), pp. 692-717. doi: 10.1177/1099636216674729.

[5] Pham, H.C., Nguyen, D.K., Nguyen, D.K., Nguyen, D.D., 2018. New approach to investigate nonlinear dynamic response of sandwich auxetic double curves shallow shells using TSDT. *Composite Structures*, 185, pp. 455–465. doi: 10.1016/j.compstruct.2017.11.047.

[6] Masters, I.G., Evans, K.E., 1996. Models for the elastic deformation of honeycombs. *Composite Structures*, 35, pp. 403-422. doi: 10.1016/S0263-8223(96)00054-2.

[7] Hedayati, R., Sadighi, M., Mohammadi Aghdam, M., Zadpoor, A.A., 2016. Mechanical properties of additively manufactured thick honeycombs. *Materials*, 9(8), pp. 613. doi: 10.3390/ma9080613.

[8] Chen, D.H., Ozaki, S., 2009. Analysis of in-plane elastic modulus for a hexagonal honeycomb core: Effect of core height and proposed analytical method. *Composite Structures*, 88(1), pp. 17–25. doi:10.1016/j.compstruct.2008.02.021.

[9] Chen, D.H., Horii, H., Ozaki, S., 2009. Analysis of In-Plane Elastic Modulus for a Hexagonal Honeycomb Core: Analysis of Young's Modulus and Shear Modulus. *Journal of Computational Science and Technology*, 3(1), pp. 1–12. doi:10.1299/jcst.3.1.

[10] Sorohan, S., Constantinescu, D.M., Sandu, M., Sandu, A.G., 2019. In-Plane homogenization of commercial hexagonal honeycombs considering the cell wall curvature and adhesive layer influence. *International Journal of Solids and Structures*, 156–157, pp. 87-106. doi: 10.1016/j.ijsolstr.2018.08.007.

[11] Montgomery-Liljeroth, E., Schievano, S., Burriesci, G., 2023. Elastic properties of 2D auxetic honeycomb structures- a review. *Applied Materials Today*, 30, 101722. doi:10.1016/j.apmt.2022.101722. 7

[12] Hohe, J., Becker, W., 2002. Effective stress-strain relations for two-dimensional cellular sandwich cores: Homogenization, material models, and properties. *ASME Appl. Mech. Rev*, 55(1), pp. 61–87. doi:10.1115/1.1425394.

[13] Wang, Z., Deng, J., Liu, K., Tao, Y., 2022. Hybrid hierarchical square honeycomb with widely tailorable effective in-plane elastic modulus. *Thin-Walled Structures*, 171, 108816. doi:10.1016/j.tws.2021.108816.

[14] Deng, J., Xu, C., Wang, X., Zhao, R., Li, T., Wang, Z., 2024. Design and optimization for honeycomb-like structures with hybridizing hierarchy and gradient strategies. *Mechanics of Advanced Materials and Structures*, pp. 1–15. doi:10.1080/15376494.2024.2429749.

[15] Wang, X., Li, Z., Deng, J., Gao, T., Zeng, K., Guo, X., Li, X., Zhai, W., Wang, Z., 2024. Unprecedented Strength Enhancement Observed in Interpenetrating Phase Composites of Aperiodic Lattice Metamaterials. *Adv. Funct. Mater*, 35, 2406890. doi:10.1002/adfm.202406890.

[16] Lan, L.H., Sun, J., Hong, F.L., Wang, D.Y., Zhang, Y.S., Fu, M.H., 2020. Nonlinear constitutive relations of thin-walled honeycomb structure. *Mech. Mater*, 149, 103556. doi: 10.1016/j.mechmat.2020.103556.

[17] Luo, L.H., Sun, W.L., Liu, J., Fu, D.Y., 2021. Analytical investigation on elastic–plastic deformation of reentrant honeycomb structures. *AIAA J*, 59(9), pp. 3735–3747. doi: 10.2514/1J060300.

[18] Zhong, R., Fu, M., Yin, Q., Xu, O., Hu, L., 2019. Special characteristics of tetrachiral honeycombs under large deformation. *International Journal of Solids and Structures*, 169, pp. 166-176. doi: 10.1016/j.ijsolstr.2019.04.020

[19] Fu, M.H., Xu, O.T., Hu, L.L., Yu, T.X., 2016. Nonlinear shear modulus of re-entrant hexagonal honeycombs under large deformation. *International Journal of Solids and Structures*, 80, pp. 284-296. doi: 10.1016/j.ijsolstr.2015.11.015.

[20] Wan, H., Ohtaki, H., Kotosaka, S., Hu, G., 2004. A study of negative poisson's ratios in

auxetic honeycombs based on a large deflection model. *European Journal of Mechanics A/Solids*, 23(1), pp. 95–106. doi: 10.1016/j.euromechsol.2003.10.006.

[21] Okereke, M.I., Akpoyomare, A.I., 2013. A virtual framework for prediction of full-field elastic response of unidirectional composites. *Computational Materials Science*, 70, pp. 82–99. doi: 10.1016/j.commatsci.2012.12.036

[22] Burlayenko, V.N., Sadowski, T., 2010. Effective elastic properties of foam-filled honeycomb cores of sandwich panels. *Composite Structures*, 92(12), pp. 2890–2900. doi: 10.1016/j.compstruct.2010.04.015.

[23] Sádaba, S., Herráez, M., Naya, F., González, C., Llorca, J., Lopes, C.S., 2019. Special-purpose elements to impose periodic boundary conditions for multiscale computational homogenization of composite materials with the explicit finite element method. *Composite Structures*, 208(15), pp. 434-441. doi: 10.1016/j.compstruct.2018.10.037.

[24] Ju, J., Summers, J.D., 2011. Compliant hexagonal periodic lattice structures having both high shear strength and high shear strain. *Materials and Design*, 32, pp. 512–524. doi: 10.1016/j.matdes.2010.08.029.

[25] Sorohan, S., Sandu, M., Constantinescu, D.M., Sandu, A.G., 2015. On the evaluation of mechanical properties of honeycombs by using finite element analyses. *Incas Bulletin*, 7(3), pp. 135–150. doi:10.13111/2066-8201.2015.7.3.13.

[26] Qiu, C., Guan, Z., Jiang, S., Li, Z., 2017. A method of determining effective elastic properties of honeycomb cores based on equal strain energy. *Chinese Journal of Aeronautics*, 30(2), pp. 766–779. doi:10.1016/j.cja.2017.02.016.

[27] Iyer, S., Alkhader, M., Venkatesh, T., 2015. Electromechanical behavior of auxetic piezoelectric cellular solids. *Scripta Materialia*, 99, pp. 65–68. doi:10.1016/j.scriptamat.2014.11.030.

[28] Khan, K., Al-Mansoor, S., Khan, S., Khan, M.A., 2019. Piezoelectric metamaterial with negative and zero Poisson's ratios. *Journal of Engineering Mechanics*, 145(10), 04019101. doi:10.1061/(ASCE)EM.1943-7889.0001674.

[29] Guo, H., Yuan, H., Zhang, J., Ruan, D., 2024. Review of sandwich structures under impact loadings: Experimental, numerical and theoretical analysis. *Thin-Walled Structures*, 196, 111541. doi:10.1016/j.tws.2023.111541.

[30] Pham, Q.-H., Tran, V.K., Tran, T.T., 2023. Vibration characteristics of sandwich plates with an auxetic honeycomb core and laminated three-phase skin layers under blast load. *Defence Technology*, Volume 24, pp. 148-163. doi:10.1016/j.dt.2022.10.002.

[31] Fang, X., Shen, H.-S., Wang, H., 2025. Nonlinear vibration analysis of sandwich plates with inverse-designed 3D auxetic core by deep generative model. *Thin-Walled Structures*, Volume 206, Part A, 112599. doi:10.1016/j.tws.2024.112599.

[32] Scarpa, F.L., Ruzzene, M., Mazzarella, L., Tsopelas, P., 2002. Control of vibration and wave propagation in sandwich plates with periodic auxetic core. *Proc. SPIE 4697, Smart Structures and Materials , Damping and Isolation*, (27 June 2002). doi:10.1117/12.472655.

[33] Hodges, D.H., Proper definition of curvature in nonlinear beam kinematics. *Ames Research Center, Moffett Field, California*. doi:10.2514/3.8861.

[34] Zohoor, H., Kakavand, F., 2012. Vibration of Euler-Bernoulli, and beams in large overall motion on flying support using finite element method, *Scientia Iranica*, 19(4), pp. 1105–1116. doi:10.1016/j.scient.2012.06.019.

[35] Dufva, K.E., Sopanen, J.T., Mikkola, A.M., 2005. A two-dimensional shear deformable beam element based on the absolute nodal coordinate formulation. *Journal of Sound and Vibration*, 3-5(280), pp. 719–738. doi: 10.1016/j.jsv.2003.12.044.

[36] Nada, A.A., Hussein, B.A., Megahed, S.M., Shabana, A.A., 2009. Use of the floating frame of reference formulation in large deformation analysis: experimental and numerical validation. *IMechE. Part K: J. Multi-body Dynamics*, 224, pp. 45-57. doi: 10.1243/14644193JMBD208.

[37] Berzeri, M., Shabana, A.A., 2000. Development of simple models for the elastic forces in the absolute nodal co-ordinate formulation. *Journal of Sound and Vibration*, 235(4), pp. 539-565. doi: 10.1006/jsvi.1999.2935.

[38] Zhang, X.S., Zhang, D.G., Chen, S.J., Hong, J.Z., 2016. Several dynamic models of a large deformation flexible beam based on the absolute nodal coordinate formulation. *Acta Phys. Sin.*, 65(9), 094501. doi:10.7498/aps.65.094501.

[39] Zhang, X., Zhang, D., Chen, S., Hong, J., 2017. Modal characteristics of a rotating flexible beam with a concentrated mass based on the absolute nodal coordinate formulation. *Nonlinear Dyn*, 88, pp. 61–77. doi:10.1007/s11071-016-3230-2.

[40] Zhao, C., Yu, H., Lin, Z., Zhao, Y., 2014. Dynamic model and behavior of viscoelastic beam based on the absolute nodal coordinate formulation. *Proceedings of the Institution of Mechanical Engineers, Part K: Journal of Multi-body Dynamics*, 229(1), pp. 84–96. doi:10.1177/1464419314548292.

[41] Shabana, A.A., Mikkola, A.M., 2003. Use of the finite element absolute nodal coordinate formulation in modeling slope discontinuity. *J Mech Des Trans ASME*, 125(2), pp. 342–350. doi: 10.1115/1.1564569.

[42] Ranjbarzadeh, H., Khalili, S.M.R., Sadati, S.H., 2025. Vibration energy harvesting using auxetic piezoelectric cellular solids. *Eng. Res. Express,* 7, 025548. doi:10.1088/2631-8695/add98d.

[43] Wang, T., Wang, L., Ma, Z., Hulbert, G.M., 2018. Elastic analysis of auxetic cellular structure consisting of re-entrant hexagonal cells using a strain-based expansion homogenization method. *Materials & Design*, 160, pp. 284 293. doi:10.1016/j.matdes.2018.09.013.